Weierstraß-Institut
für Angewandte Analysis und Stochastik

Leibniz-Institut im Forschungsverbund Berlin e. V.

Preprint ISSN 2198-5855

Dynamics in high-power diode lasers

Uwe Bandelow[1], Mindaugas Radziunas[1], Anissa Zeghuzi[2],

Hans-Jürgen Wünsche[1,2], Hans Wenzel[2]

submitted: April 15, 2020

[1] Weierstrass Institute
Mohrenstr. 39
10117 Berlin
Germany
E-Mail: uwe.bandelow@wias-berlin.de
mindaugas.radziunas@wias-berlin.de
hans-juergen.wuensche@wias-berlin.de

[2] Ferdinand-Braun-Institut
Leibniz Institut für Höchstfrequenztechnik
Gustav-Kirchhoff-Straße 4
12489 Berlin
Germany
E-Mail: anissa.zeghuzi@fbh-berlin.de
hans-juergen.wuensche@fbh-berlin.de
hans.wenzel@fbh-berlin.de

No. 2715
Berlin 2020

2010 *Mathematics Subject Classification.* 78A60, 35Q60, 78-04, 35Q79, 35B35.

Key words and phrases. High-power diode lasers, thermal lensing, laser dynamics, heating, filaments.

This work has been supported by the German Federal Ministry of Education and Research (BMBF) contract 13N14005 as part of the EffiLas/HoTLas project.

Edited by
Weierstraß-Institut für Angewandte Analysis und Stochastik (WIAS)
Leibniz-Institut im Forschungsverbund Berlin e. V.
Mohrenstraße 39
10117 Berlin
Germany

Fax: +49 30 20372-303
E-Mail: preprint@wias-berlin.de
World Wide Web: http://www.wias-berlin.de/

Dynamics in high-power diode lasers

Uwe Bandelow, Mindaugas Radziunas, Anissa Zeghuzi,
Hans-Jürgen Wünsche, Hans Wenzel

Abstract

High-power broad-area diode lasers (BALs) exhibit chaotic spatio-temporal dynamics above threshold. Under high power operation, where they emit tens of watts output, large amounts of heat are generated, with significant impact on the laser operation. We incorporate heating effects into a dynamical electro-optical (EO) model for the optical field and carrier dynamics along the quantum-well active zone of the laser. Thereby we effectively couple the EO and heat-transport (HT) solvers. Thermal lensing is included by a thermally-induced contribution to the index profile. The heat sources obtained with the dynamic EO-solver exhibit strong variations on short time scales, which however have only a marginal impact on the temperature distribution. We consider two limits: First, the static HT-problem, with time-averaged heat sources, which is solved iteratively together with the EO solver. Second, under short pulse operation the thermally induced index distribution can be obtained by neglecting heat flow. Although the temperature increase is small, a waveguide is introduced here within a few-ns-long pulse resulting in significant near field narrowing. We further show that a beam propagating in a waveguide structure utilized for BA lasers does not undergo filamentation due to spatial holeburning. Moreover, our results indicate that in BALs a clear optical mode structure is visible which is neither destroyed by the dynamics nor by longitudinal effects.

1 Introduction

Due to their small size and high efficiency broad-area (BA) lasers are important pump sources for high-performance laser systems and are also used for direct material processing. Tens of watts output from single devices can be obtained. Not to exceed the critical intensity for catastrophical facet degeneration, the beam area at the facet must be large and the intensity distribution should be as flat as possible. This gives rise to multimode operation, such that mode beating is unavoidable. The inherent nonlinearities transform this beating into a rather complex spatio-temporal behaviour. In the present paper we describe a numerical tool that is able to accurately calculate these phenomena. It considers all essential elements of realistic device structures but is still simple enough for design optimizations within reasonable computing times. The developed simulation tool BALaser bases on sophisticated numerical algorithms [1, 2, 3, 4]. Applications to several subjects have been reported, among them different types of beam shaping and stabilization [5, 6, 7], as well as tailoring external feedback [8, 9]. We cannot present all this work here, but focus on two further applications: i) what is the nature of filamentation [10] and ii) which role possible temporal changes of temperature are playing[11]?

In optics, the notion *filamentation* means the creation of a self-trapped beam of light in a nonlinear medium or the breakup of a beam into many transverse components [12], Ch.7, p. 330. BA lasers typically show beam break up as in the example of Fig. 1(a). Since this example is calculated with our model, we can ask for the nature of this effect. In literature it is often discussed along the idea of the modulation instability of a beam in a medium with a Kerr nonlinearity. We have evaluated this idea

DOI 10.20347/WIAS.PREPRINT.2715 Berlin 2020

on base of our model. The results agree exactly with theory in case of an ideal homogeneous Kerr medium. However, we do not find an indication of the modulation instability for realistic device structures. Instead, the filamentation is structured here by the transverse modes of the cavity. Moreover, the filaments of the time-averaged intensity are highly dynamical objects as the snapshot of Fig. 1(b) demonstrates. Here we see chaotic light bullets rather than filaments. Note, however, the different axis scales. The bullets are hundreds microns long but only few microns wide. They are a kind of short filaments flying through the device.

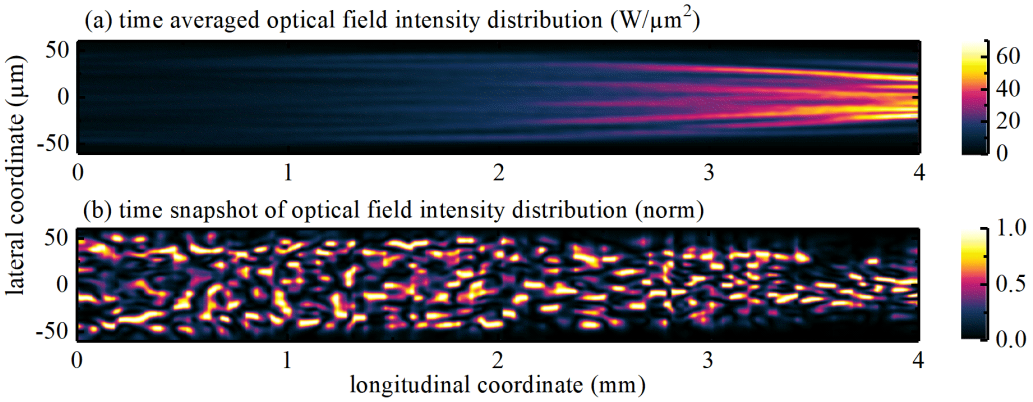

Figure 1: Top view on the optical intensity distribution in the active region of the BA laser of Fig. 2 under continuous wave (CW) high power operation, calculated with the model of section 2. (a) time averaged, (b) time snapshot of intensities laterally normalized at each longitudinal position.

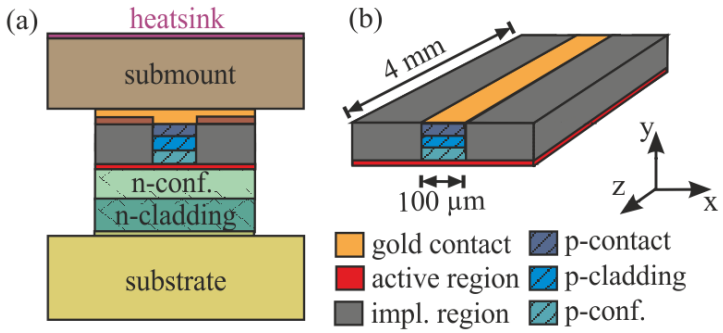

Figure 2: Sketches of a typical BA laser. (a) Vertical-lateral cross section of the thermal simulation domain. (b) Domain of the electro-optical simulation. Our calculated example device has rear and front facet power reflectivities of $R_0 = 0.95$ and $R_L = 0.01$, respectively. The active layer consists of a 7-nm-thick single InGaAs quantum well embedded in p- and n-doped AlGaAs cladding and optical-confinement layers. To provide lateral current confinement the p-doped layers are implanted down to the vicinity of the active region. The vertical layer structure is designed to form an index-guided single-mode large-optical-cavity waveguide with negligible carrier accumulation in the confinement and cladding layers.

A large amount of heat is generated in high-power lasers. Even being cooled, the interior temperature is increased with large impact on the laser operation. The most prominent effect is the formation of a thermally induced waveguide, i.e. a substantial increase of the refractive index in the hot center below the contact stripe, commonly referred to as thermal lens. In the example of Fig. 1, it causes a slight focussing close to the right facet. Thermal lenses are well studied for continuous wave (CW) operation and a steady temperature distribution. They are usually neglected under pulsed operation because

thermal build-up times up to milliseconds are much longer than the pulse lengths. However, the heat is generated near to the active layer in the same region where the guided wave is localized. This region is small and its thermal build-up time is much shorter than that of the whole device. Thus, one can also expect focussing, but with a dynamic thermal lens.

Short-time local heating can be expected to influence the optical pulse formation although time-averaged heating is negligible. Theoretically, a time-dependent temperature has been considered in early models as presented e.g. in Refs. [13, 14]. They concentrated on a sophisticated microscopic description of the processes in the active layer. However, besides requiring enormous computer resources even for nanosecond transients, they disregarded outer parts of devices, where a considerable portion of the heat is generated. Heat flow was replaced by a simple local relaxation of temperature towards an ambient temperature. These features limit applications in device design.

Our paper is structured as follows. The time-dependent quasi three-dimensional electro-optic-thermal model is presented in Section 2. It bases on our previous electro-optical model and solver BALaser [15, 16, 17]. Its upgrade with a space-time dependent thermal model is designed so that few-nanoseconds-long transients can be calculated within minutes. As a first application, the nature of filamentation in such devices is explored in Section 3. Exemplary laser operation with 10 ns long pulses is simulated in section 4, revealing a fast-growing thermally induced waveguide initializing the known stationary thermal lens. The paper is summarized in section 5.

2 The electro-optical and thermal model

2.1 Electro-optical model of the active layer

Our mathematical model is a hybrid combination of a traveling-wave (TW) model in the (x, z) plane, a model of current flow in the (x, y) plane, and a thermal model. In the semiclassical framework of rotating-wave, scalar, effective-index and paraxial approximations, the transverse-electric optical field is represented by its electric x-component

$$E(\vec{r}, t) = A\,\phi(y)\left[u^{+}\mathsf{e}^{-i\bar{n}k_0 z} + u^{-}\mathsf{e}^{i\bar{n}k_0 z}\right]\mathsf{e}^{i\omega t} + c.c. \tag{1}$$

with $A = \sqrt{d\hbar\omega/(2\epsilon_0\bar{n}n_g)}$ and $k_0 = 2\pi/\lambda_0$. $\lambda_0 = 910$ nm, $d = 7$ nm, $\hbar$, ϵ_0, $n_g = 3.87$, $\bar{n} = 3.4$, ω and c are the center wavelength, the thickness of the active region, the Planck constant, the vacuum permittivity, the group refractive index, a real valued reference index, a reference angular frequency and the vacuum speed of light, respectively. Supposing a well-designed vertical waveguide, the normalized fundamental vertical mode $\phi(y)$ is calculated in advance for the cold cavity and remains unchanged. The slowly varying complex amplitudes $u^{\pm}(x, z, t)$ obey a traveling wave equation (TWE) coupled to a diffusion equation for the carrier density $N(x, z, t)$ (sheet density divided by the QW thickness)

$$\left[\frac{1}{v_{\mathsf{g}}}\frac{\partial}{\partial t} \pm \frac{\partial}{\partial z} + \frac{i}{2\bar{n}k_0}\frac{\partial^2}{\partial x^2} + \mathcal{D}\right] u^{\pm} = -ik_0\left[\Delta n_{\mathsf{eff}}(N, T, \|u\|^2) + \Delta n^{\pm}_{2,\mathsf{eff}}(|u^{\pm}|^2)\right] u^{\pm} + f^{\pm}_{\mathsf{sp}}, \tag{2}$$

$$\frac{\partial N}{\partial t} = \frac{\partial}{\partial x}\left(D_{\mathsf{eff}}(N)\frac{\partial N}{\partial x}\right) + \frac{j(x, z, t)}{ed} - R(N, u^{\pm}, \mathcal{D}). \tag{3}$$

Here, $j(x, z, t)$ is the injection current density, $\|u\|^2 = |u^{+}|^2 + |u^{-}|^2$ the local photon density, D_{eff} an effective diffusion coefficient and $R(N, u^{\pm}, \mathcal{D}) = AN + BN^2 + CN^3 + R_{\mathsf{stim}}(N, u^{\pm}, \mathcal{D})$ the

recombination rate, where A, B, C are the Shockley-Read-Hall, spontaneous radiative and Auger recombination coefficients.
The rate of stimulated recombination $R_{stim}(N, u^{\pm}, \mathcal{D}) = v_g Re \sum_{\nu=\pm} u^{\nu *}(g - 2\mathcal{D})u^{\nu}$ is mainly determined by the term $v_g g(x, z, N, \|u\|^2)\|u\|^2$. The local carrier density-dependent gain g accounts also for nonlinear gain compression: $g = g' \log(N/N_{\rm tr})/(1 + \varepsilon_{\rm s}\|u\|^2)$, with g', $N_{\rm tr}$ and $\varepsilon_{\rm s}$ as differential modal gain, transparency carrier density and gain compression factor, respectively. The operator $\mathcal{D}$ is used to model dispersion of the optical gain [18]. We use it in the form

$$\mathcal{D}u^{\pm} = \frac{g_r}{2}(u^{\pm} - p^{\pm}), \quad \frac{\partial p^{\pm}}{\partial t} = \gamma(u^{\pm} - p^{\pm}) + i\delta\omega p^{\pm}, \tag{4}$$

which couples the traveling wave equations (2) to ordinary differential equations for the complex slowly varying amplitudes of the polarization fields $p^{\pm}$ [18]. This approximates the dispersion of the gain with a Loretzian of amplitude g_r, half width at half maximum γ, and relative central frequency $\delta\omega$.

The amplitudes $u^{\pm}$ are coupled to each other by reflecting boundary conditions at the facets. Periodic boundary conditions are assumed at the lateral boundaries of the sufficiently broad simulation domain. The complex effective index deviation $\Delta n_{\rm eff}$ from the reference index $\bar{n}$ obeys

$$\Delta n_{\rm eff}(x, z, N, T) = \Delta n_0(x, z) + \Delta n_{\rm N}(x, z, N) + \Delta n_{\rm T}(x, z, T) + {\rm i}\frac{g(x, z, N, \|u\|^2) - \alpha(x, z, N)}{2k_0}, \tag{5}$$

with Δn_0, $\Delta n_{\rm N}$, and $\Delta n_{\rm T}$ accounting for built-in index changes, carrier density and temperature dependent index changes, respectively, and α for optical loss, which includes effective internal background absorption and free carrier absorption in the active region. $\Delta n^{\pm}_{\rm 2eff}$ describes effective changes of the complex refractive index due to the Kerr effect $\Delta n^{\pm}_{\rm 2r}$ and two-photon absorption $\alpha^{\pm}_{\rm 2P}$ and is derived as

$$\Delta n^{\pm}_{\rm 2eff} = \Delta n^{\pm}_{\rm 2r} - i\frac{\alpha^{\pm}_{\rm 2P}}{2k_0} = \left(n'_2 - i\frac{\beta'}{2k_0}\right)\hbar\omega_0 v_g d(\|u\|^2 + |u^{\mp}|^2), \tag{6}$$

with the effective optical Kerr coefficient n'_2 in units of mW^{-1} and the effective two-photon absorption coefficient β' in units of W^{-1} [19].

The thermally induced index, that will be used later

$$\Delta n_T(T) = \int n'_T T|\phi|^2 dy \tag{7}$$

with constant slope parameters n'_T in each material, is the main impact of temperature variations on the wave propagation. Thermal changes of the Fermi distribution functions are also taken into account.

The numerical integration of the TW-model equations presented above are performed using parallel computing and distributed memory paradigm (MPI) at the WIAS in Berlin. Typical 1 ns-transient simulations of 4 mm-long and 100 um-broad laser using 20-30 parallel processes can be made in 5-10 minutes. More details on the efficiency of the code are given in [16].

2.2 The (x, y) model of current flow through the p-layers

Current spreading and current self-distribution in the p-doped layers play an important role in BA lasers [3, 11]. They are also expected to have a large impact on the Joule heating, which is proportional to the square of the current density,

$$\vec{j} = \sigma\nabla\varphi_p \tag{8}$$

with the electrical conductivity σ. The quasi-Fermi potential φ_p of the holes is determined by solving a Laplace equation in the p-doped region [3, 7],

$$\nabla(\sigma\nabla\varphi_p) = 0 \tag{9}$$

with the boundary conditions $\varphi_p|_{y=y_a} = \varphi_F(N,T)$ at the active layer, $\varphi_p = U$ at the p-contact, and $\frac{\partial}{\partial n}\varphi_p = 0$ elsewhere, where $\frac{\partial}{\partial n}$ is the normal derivative. U is the bias voltage and $\varphi_F(N,T)$ is the Fermi voltage in the active layer, i.e. the separation between the quasi-Fermi potentials of holes and electrons. The injection current density $j(t,x,z)$ entering equation (3) is the y-component of $\vec{j}$ at the upper boundary of the active layer adjacent to the p-doped region. To numerically solve the presented equations the scheme extensively described in Ref. [3] is applied.

2.3 The thermal model

The heat model calculates the heat generation using results of the opto-electronic model, solves the heat-flow equation, and determines the thermal index contribution (7) acting on the wave propagation.

2.3.1 Heat generation

The heat sources of the model that we list now, are derived from corresponding expressions given in [20, 21].

In accordance with the current flow model the Joule heat

$$h_{\mathsf{J}} = j_p^2/\sigma \tag{10}$$

is essentially generated in the p-doped region and can be neglected in the n-doped region, due to the very high electron conductivity.

The heat source due to absorption of stimulated emitted photons is given as

$$h_{\mathsf{abs}} = \begin{cases} v_g\hbar\omega d\frac{n(y)}{\bar{n}}|\phi(y)|^2\|u(x,z,t)\|^2\left[\alpha_0(y)+v_g\hbar\omega d\beta_{\mathsf{2P}}(y)|\phi(y)|^2\|u(x,z,t)\|^2\right], & y\notin \mathsf{AR},\\ v_g\hbar\omega f_N N\|u(x,z,t)\|^2, \quad y\in \mathsf{AR} \end{cases} \tag{11}$$

where the abbreviation AR denotes the active region, $n(y)$, $\alpha_0(y)$ and $\beta_{\mathsf{2P}}(y)$ are the vertical distribution of the real part of the refractive index, the absorption and the 2-photon absorption coefficient, respectively. The first term in equation (11) accounts for background absorption due to doping, the second term denotes 2-photon-absorption in the cladding and confinement layers, whereas the term in the second line of equation (11) is due to free carrier absorption in the active region. [1]

The third source term is recombination heat in the active region,

$$h_{\mathsf{rec}} = e\varphi_F(N,T)(AN + \xi BN^2 + CN^3) \tag{12}$$

where ξ denotes the portion of absorbed spontaneous emission. By setting $\xi = 1$ we have assumed, that all spontaneous emission is transferred into heat and not to the radiation field.

[1] Note that for $\alpha_{0,\mathsf{eff}}$ and f_{2P} entering the effective absorption coefficient of the traveling wave equation, $\alpha_{0,\mathsf{eff}} = \int n(y)\alpha_0(y)/\bar{n}|\phi|^2dy$ and $f_{\mathsf{2P}} = \hbar\omega v_g d_a \int n(y)\beta_{\mathsf{2P}}(y)/\bar{n}|\phi|^2dy$ must hold[22].

The last term taken into account denotes quantum defect heat generated in the active region as a result of incomplete energy transfer from the carrier reservoir to the radiation field, given as

$$h_{\text{defect}} = (e\varphi_F(N,T) - \hbar\omega)R_{\text{stim}}(N, \|u\|^2). \tag{13}$$

Furthermore, in this paper we neglect Thompson-Peltier heat [20, 21] as the overall impact is expected to be small[22].

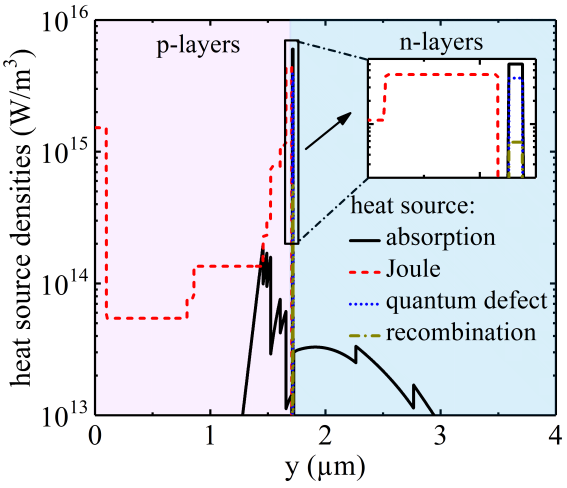

Figure 3: Time averaged absorption, Joule, recombination and quantum defect heat source densities as function of the vertical y-direction in the middle of the stripe.

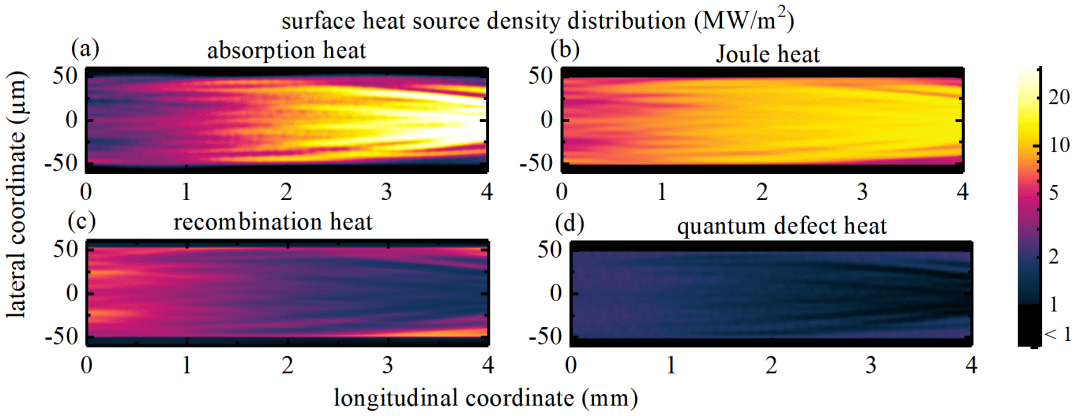

Figure 4: Distribution of the time-averaged (a) absorption, (b) Joule, (c) recombination, and (d) quantum defect surface heat source densities $H = \int h dy$ as function of lateral and longitudinal (x, z)-coordinate.

2.3.2 Heat flow equations

Our model bases on the classical macroscopic heat-flow equation,

$$c_{\text{h}}\frac{\partial T}{\partial t} - \nabla\left[\kappa_{\text{L}}\nabla T\right] = h(N, \vec{j}, \|u\|^2), \tag{14}$$

with the heat capacity c_{h}, the heat conductivity κ_{L}, the heat source

$$h = h_{\text{J}} + h_{\text{abs}} + h_{\text{rec}} + h_{\text{defect}}, \tag{15}$$

with the individual heat sources given in equations (10) - (13) and the boundary conditions

$$\begin{array}{rcll} \kappa_L \frac{\partial}{\partial n} T & = & -(T - T_{\mathsf{HS}})/r_{\mathsf{th}} & \text{for } (x,y,z) \in \text{heat sink} \\ \frac{\partial}{\partial n} T & = & 0 & \text{for } (x,y,z) \in \text{other outer bounds} \end{array} \tag{16}$$

where r_{th} is the thermal resistivity. Here and in what follows, T is the absolute temperature and T_{HS} the temperature of the heat sink, which also serves as reference for parameter values. The arguments of h on the right hand side of equation (14) symbolize that the heat source power densitiy h depends on the carrier density, current density, and field intensity distributions in the laser, which result from the opto-electronic model. Reversely, T acts back on the wave propagation mainly via the thermally induced effective index (7). In addition, T implicitly influences the gain, distribution functions, and the diffusion as well as recombination terms in equation (3). Thermal changes of parameters are disregarded in this paper, in order to separate those from thermal wave-guiding effects.

Short times: the no-heat-flow (NHF) approximation It is unreasonable to solve the heat-flow equation (14) over tens of microseconds with the sub-ps temporal resolution of the opto-electronic model in the large spatial domain sketched in Fig. 2(b). Fortunately, the following inherent features of heat generation and transport enable us to simplify the problem considerably. Most of the heat is generated in the active layer or very close to it (Fig. 3). During a given time τ, it flows only into a finite region of size l which is related to τ by the inverse thermal diffusivity,

$$\frac{\tau}{l^2} \approx \frac{c_h}{\kappa_L} \approx 10^5 \,\mathsf{s/m}^2 \approx \frac{1 \,\mathsf{ns}}{(100 \,\mathsf{nm})^2}. \tag{17}$$

Thus, the generated heat during a 1 ns simulation interval is spread by only about 100 nm. This distance is much smaller than transverse inhomogeneities of the heat source density, see Fig. 4. It is also smaller than the vertical extension of the mode profile $|\phi(y)|^2$ as is visible in Fig. 12(a) and does only marginally affect the thermally induced index (7). Heat flow is therefore negligible when simulating short transients. Differentiating (7) with respect to time and inserting (14) with $\kappa_L = 0$, we find the ordinary differential equation

$$\frac{\partial \Delta n_T}{\partial t} = \int \frac{n_T'}{c_{\mathsf{h}}} |\phi(y)|^2 h(N, \vec{j}, \|u\|^2) dy \tag{18}$$

for the thermally induced index. It is integrated much easier in each node of the spatial grid than the original partial differential heat-flow equation (14).

Treatment of CW operation The extremely long thermal build up in the case of CW operation cannot be calculated with the NHF approximation. But in the later quasi-steady state, the rate of heat generation can be decomposed in a time-constant mean contribution $\bar{h}$ and a contribution $h_{\mathsf{fluct}} = h - \bar{h}$ fluctuating around zero. h is the total instantaneous heat production (15). Accordingly, the heat-flow equation (14) is split into

$$0 = \nabla \kappa_L \nabla \bar{T} + \bar{h} \qquad \text{and} \tag{19}$$

$$c_h \frac{\partial T_{\mathsf{fluct}}}{\partial t} = \nabla \kappa_L \nabla T_{\mathsf{fluct}} + h_{\mathsf{fluct}} \tag{20}$$

with boundary conditions following from (16). The heat capacity c_{h} and the heat conductivity κ_{L} may vary in space but not in time. Obviously, the sum of the two temperatures obeys the full heat-flow

equation (14). The time scale of the fluctuations $h_{\text{fluct}} = h - \bar{h}$ is typically in the sub-ns range. Thus, equation (20) is solved with the NHF approximation (18) along a few-ns long simulation interval. Treating the stationary equation (19) is more challenging because heat flow dominates and it must be solved in the full domain of the vertical structure including submount and substrate, Fig. 2(b). Furthermore, the mean heat production $\bar{h}(x, y, z)$ is not known in advance. Therefore, we apply an iterative approach. In the first step of the iteration the electro-optic model is solved under isothermal conditions with $T = T_{\text{HS}}$. During this run, we set $\bar{h} = 0$. In all following iterations, $\bar{h}$ is taken as the temporal average of the total heat production of the last part of the iteration before and the fluctuating part inserted into (18) is h_{fluct}. The iterations are repeated until the temperature and near-field intensity distributions of consecutive iteration steps are sufficiently close to each other. A detailed description of the numerical implementation is given in Ref. [4].

3 Application I: nature of filamentation

BA lasers typically show lateral modulations of the intensity as in the example of Fig.1a. In literature this phenomenon is usually named filamentation in analogy to the filamentation of a beam in a medium with a Kerr nonlinearity. We have evaluated this idea in more detail. Essentials are presented here, details are found in Ref.[10]. We start with considering an ideal Kerr medium. The theoretical understanding of beam breakup due to a modulation instability is summarized in subsection 3.1. Subsection 3.2 demonstrates that our software exactly reproduces this theory for a fictive Kerr medium. Unfortunately, the Kerr coefficients of our semiconductor material are too small and have the wrong sign to cause this effect. However, it has been argued that spatial hole burning (SHB) gives rise to an effective Kerr coefficient of right sign and sufficient magnitude. We simulate a fictive Kerr medium with this coefficient but do not find filamentation in subsection 3.3. Finally, in subsection 3.4, we show that the lateral modulation of the intensity is governed by a finite number of transverse modes that carry the lasing process.

3.1 Filamentation: elementary theory for homogeneous beams

Beam breakup can happen in a medium with a focusing Kerr nonlinearity as a consequence of the growth of spatial irregularities initially present on the laser wavefront [12]. The elementary theory of this modulation instability has been formulated in the sixties by Bespalov and Talanov [23]. A monochromatic spatially nearly homogeneous beam is injected into the medium at $z = 0$. Within our framework, suppressing the superscript +, the governing equation for its further propagation following from Eq. (2) is the Nonlinear Schrödinger Equation (NLS)

$$\left[\frac{\partial}{\partial z} + \frac{i}{2\bar{n}k_0}\frac{\partial^2}{\partial x^2}\right] u(x,z) = -ik_0 n_2' \hbar\omega_0 v_{\text{g}} d \|u(x,z)\|^2 u(x,z), \;\; u(x,0) = u_0 + \delta u_0(x), \quad (21)$$

where $\delta u_0(x)$ is an infinitesimally small deviation from spatial homogeneity. Along a certain distance, the solution can still be expressed as sum of a strong plane wave component and a small perturbation,

$$u(x,z) = (u_0 + \delta u(x,z)) \cdot e^{-i\kappa z} \qquad \text{with } \kappa = k_0 n_2' \hbar\omega_0 v_g d|u_0|^2 \text{ and } \delta u(x,0) = \delta u_0(x). \quad (22)$$

Linearizing Eq. (21) with respect to a small perturbation with lateral wavenumber q, one finds[12]

$$\delta u(x,z) = u_1 e^{-i(qx+\gamma z)} + u_{-1}^* e^{i(qx+\gamma^* z)} \quad (23)$$

with

$$\gamma = \pm \frac{q}{2\bar{n}k_0} \sqrt{q^2 - 4\bar{n}k_0^2 n_2' \hbar\omega v_g d \|u_0\|^2}. \tag{24}$$

Thus, long-wave perturbations with $q < q_{\text{crit}}$,

$$q_{\text{crit}} = \sqrt{4\bar{n}k_0^2 n_2' \hbar\omega v_g d \|u_0\|^2}, \tag{25}$$

will be amplified, which happens only for focussing Kerr media with positive real values of n_2'. Fourier components with different q possess different exponents γ, as an example see the black curve in Fig. 5(a). Those with the maximum imaginary part $\gamma_{\text{max}} = \max(\Im m[\gamma])$ at $q = q_{\text{opt}}$ grow fastest. They will dominate after a certain path compared to other Fourier components. At this stage, the beam is laterally modulated with a period $\Lambda_{\text{opt}} = 2\pi/q_{\text{opt}}$. This is the elementary process of beam breakup in a homogeneous medium.

3.2 Filamentation: simulation of finite width effects

BA lasers have waveguides of finite width W. Thus, laterally homogeneous beams cannot propagate and the described elementary theory is not applicable. To circumvent this aspect, we consider here waveguides with laterally periodic boundary conditions. The above theory is now applicable, only the lateral wave vectors are limited to integer multiples of $2\pi/W$. We consider an example with following parameters: simulation domain $W = 400$ µm, power density $\hbar\omega v_g |u_0|^2 = 100$ W/µm^2, and $n_2' = 10^{-11}$ mW^{-1}. This power density can be achieved under pulsed operation. The Kerr coefficient is artificially large to demonstrate the effects. Its relation to the real world will be discussed at the end.

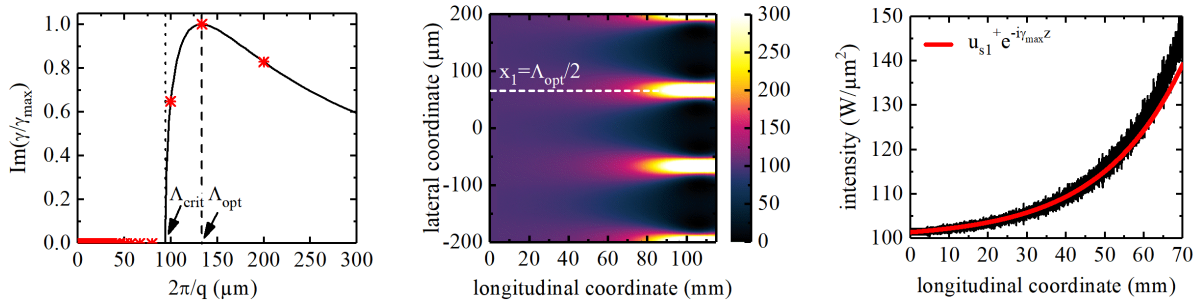

(a) prediction from Eq. (24) (b) forward field intensity (W/µm^2) (c) field intensity at $x_1 = \Lambda_{\text{opt}}/2$

Figure 5: Theoretical prediction and numerical experiment using the traveling wave simulation of the forward field intensity while propagating in an isotropic nonlinear dielectric with average material Kerr coefficient $n_2' = 10^{-11}$ m/W and originally injected field intensity of $\hbar\omega v_g \|u_{s00}^+\|^2 \approx 100$ Wµm^{-2} including small random perturbations $\delta u_s^+(x,z)$. (a) Theoretical prediction of $\text{Im}(\gamma/\gamma_{\text{max}})$ as function of the lateral period $2\pi/q$, Eq. (24). The vertical dotted line indicates the shortest period Λ_{crit} at which instabilities occur. The vertical dashed line indicates the optimum period Λ_{opt} for perturbations to grow. Red asterisks indicate allowed values for a total simulation domain of $W = 400$ µm. (b) Longitudinal-lateral distribution of the forward field intensity. (c) Forward propagating field intensity at position $x_1 = \Lambda_{\text{opt}}/2$ and theoretical development of $u_{s1}^+ e^{-i\gamma_{\text{max}} z}$ with a filament gain of $\gamma_{\text{max}} = (21 \text{ mm})^{-1}$.

For this model case Fig. 5(a) shows the dependence of $\text{Im}(\gamma/\gamma_{\text{max}})$ on the period of the perturbation $2\pi/q$. The allowed periods for $W = 400$ µm are shown as red asteriscs. Only three of them are above

the critical $\Lambda_{\text{crit}} = 94$ µm. The expected distance between filaments is $\Lambda_{\text{opt}} = 133$ µm, which is one third of the stripe width in the present case. The gain of these optimum filament embryos is $\gamma_{\text{max}} = (21\text{ mm})^{-1}$, which characterizes the necessary propagation distance for its possible observation.

Now we check whether our numerical model is in agreement with these predictions. The resulting longitudinal-lateral field intensity distribution is visible in Fig. 5(b). Clear filaments with a spacing that exactly corresponds to Λ_{opt} are observed. Furthermore Fig. 5(c) shows the field intensity at position $x_1 = \Lambda_{\text{opt}}/2$ together with the theoretical development of $\hbar\omega v_g |u(x_1, z)|^2$ according to Eq. (22). For longitudinal distances $z < 50$ mm the theoretical estimation corresponds very well to the results of the numerical traveling-wave model. However, the more the filament intensities grow, the more both curves differ due to deviations from linearity.

For the focusing NLS (21) within infinite domain $-\infty < x < \infty$ the general solution to this problem is given by the class of Akhmediev Breathers [24]. This is a multi-parameter family of analytic solutions to (21), where the free parameters can be used to adjust the period of the Akhmediev Breather, such that the periodic situation here is covered by these solutions. In the extreme case where the period tends to infinity we end up with the famous Peregrine soliton, which is a rational solution of (21) [25].

Concluding so far, our numerical traveling wave simulation describes very well the filamentation due to a focussing Kerr nonlinearity. Unfortunately, the relevant material Kerr coefficients in our lasers are negative and cannot be responsible for filamentation.

3.3 Filamentation due to spatial hole burning?

In semiconductor lasers an effective Kerr-nonlinearity can however be induced by spatial hole burning due to the dependence of the refractive index on the carrier density [26]. Early results of simulations based on a Maxwell-Bloch type dynamic traveling-wave model with a sophisticated treatment of carrier kinetics supported this view [27]. For a hypothetical steady state the effective Kerr coefficient is [28, 19]

$$n_2' = -\left[\alpha_{\text{H}} g' + i(g' - \alpha')\right] \frac{(j - j_{\text{tr}})\ g' \tau_N^2}{2ek_0 \hbar\omega_0 d^2}. \tag{26}$$

The prime denotes derivative with respect to N at transparency. $j_{\text{tr}} = edN_{\text{tr}}/\tau_N$, $\alpha_{\text{H}} = 2k_0 \Delta n_N'/g'$, and τ_N are the transparency current density, Henry's linewidth enhancement factor, and the recombination life time, respectively [19]. With the parameters of our devices[19], a typical current density $j = 5 \cdot 10^7$ A/m^2 and a field intensity of $\hbar\omega v_g \|u_{s00}^+\|^2 \approx 10$ W µm^{-2} we get Real$(n_2') = 3.6 \cdot 10^{-6}$ m/W. This is much larger than the fictive material coefficient used above in subsection 3.2. Thus it is not surprising that the characteristic length scales of filamentation are much smaller, Fig. 6(a). The expected length of formation of filaments is only $\gamma_{\text{max}}^{-1} = 500$ nm. The critical and optimum periods are $\Lambda_{\text{crit}} = 0.5$ µm and $\Lambda_{\text{opt}} = 0.7$ µm, respectively. Both values are further decreasing with current, Fig. 6(b). Accordingly we should expect a very effective formation of filaments.

To check these predictions, we perform with these parameters a similar numerical experiment as in last subsection. Since length scales are smaller, we choose a width $W = 20$ µm. Using the idealized stationary Eq. (21) with the real part of the Kerr coefficient (26) yields the expected filamentation. Surprizingly, no filamentation shows up when applying the full time-dependent equations (2 to 4). Instead, the injected beam propagates with constant intensity plus tiny ripples, Fig. 6(c). The expected growth of filaments is suppressed mainly by two effects. First, the length scale of possible filaments is much smaller than the diffusion length. Thus, diffusion washes out the carrier depletions. Second, light is less amplified in a region with depleted carriers, and reversely outside of such regions. This effect balances the intensities counteracting the filamentation. Irrespective of the details it can be con-

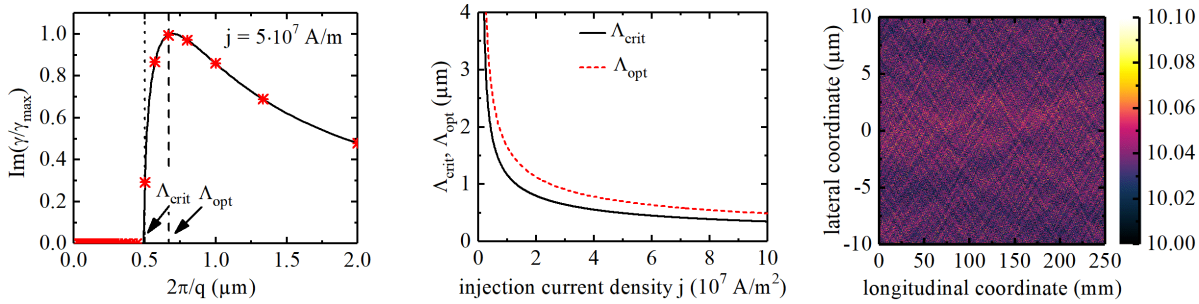

(a) $\mathrm{Im}(\gamma/\gamma_{\mathrm{max}})$ as function of $2\pi/q$ (b) Λ_{crit} and Λ_{opt} as function of j (c) taveling-wave simulation

Figure 6: Theoretical prediction and numerical experiment using the traveling wave simulation of the forward field intensity while propagating through a semiconductor slab waveguide with an equivalent Kerr coefficient of $n_2' = 3.6 \cdot 10^{-6}$ m/W obtained for an injection current density of $j = 5 \cdot 10^7$ A/m^2. An originally injected field intensity of $\hbar\omega v_g \|u_{s00}^+\|^2 \approx 10$ Wμm^{-2} including small random perturbations $\delta u_s^+(x,z)$ is assumed. (a) Filament gain $\mathrm{Im}(\gamma/\gamma_{\mathrm{max}})$ as function of period $2\pi/q$. Critical and optimum period are indicated by vertical lines. Red asterisks indicate allowed values for a total simulation domain of $W = 4$ μm. (b) Critical period Λ_{crit} (black solid) and optimum period Λ_{opt} (red dashed) as function of the injection current density j. (c) Traveling wave simulation of the forward field intensity propagating though a semiconductor gain material with W=20 μm and an averaged carrier density of $\bar{N} = 3 \cdot 10^{24}$ m^{-3} for which the modal gain is compensated for by the absorption ($g(\bar{N}) = \alpha(\bar{N})$).

cluded that filamentation of an injected beam by spatial hole burning does not occur in the waveguide structures used for BA lasers.

3.4 The mode picture of dynamical filamentation

If not a Kerr-type filamentation, what else is the reason for the lateral structure of the intensity in a BA laser as examplified in Fig. 1? We shall demonstrate that this behavior can be better understood in terms of lateral modes [11]. We simulate a laser with the parameters of Ref. [11]) at an exemplary constant pump current above threshold. After turn-on oscillations, the time traces of output power and intensity profiles at the front facet behave as shown in Figs. 8(a) and (b). A highly dynamic behavior is visible. In panel (b) lateral structures with different numbers of intensity peaks can be identified that merge into each other over time. They can be interpreted as lateral modes that dominate during a finite time until other modes take over. In order to explore this presumption, we perform a mode analysis. To this purpose, the complex-valued field profile at the front facet, $z = L$, and a given instantaneous time t is expanded in terms of the modes $\phi_m(x)$ of the Helmholtz equation for a hypothetical steady state,

$$\left[k_0^{-2}\partial^2/\partial x^2 + \langle n_{\mathrm{eff}}(x)\rangle_t^2\right]\phi_m(x) = \hat{n}_m^2\phi_m(x), \tag{27}$$

where x is the lateral coordinate, $\hat{n}_m$ is the modal index being the complex-valued eigenvalue and $\langle n_{\mathrm{eff}}(x)\rangle_t^2 = [\bar{n} + \langle \Delta n_{\mathrm{eff}}(x)\rangle_t]^2$ the time averaged effective index, which includes the same built-in modifications of the effective index, carrier induced index contributions as well as gain and losses as the traveling wave model and is calculated from the time averaged profiles of carrier density $\langle N\rangle_t$ and field intensity $\langle \|u\|^2\rangle_t$. The imaginary and real parts of the eigenvalues of (27) are displayed in Fig. 7 where the ordinate is the modal gain $g_m = 2k_0\mathrm{Im}(\hat{n}_m)$ and the abscissa the real part of the modal index relative to the real part of the index of the fundamental mode, $\Delta\mathrm{Re}(\hat{n}_m) = \mathrm{Re}(\hat{n}_m) - \mathrm{Re}(\hat{n}_1)$. For every time instance the complex optical field amplitude $u_{\mathrm{out}}(x,t)$ emitted at the front facet can be

expressed as a linear combination of the eigenfunctions ϕ_m of (27),

$$u_{\text{out}}(x,t) = \sum_m a_m(t)\phi_m(x,t), \qquad a_m = \frac{\int \phi_m u_{\text{out}}\, dx}{\int \phi_m \phi_m\, dx}. \tag{28}$$

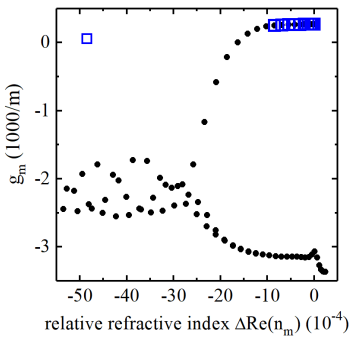

Figure 7: Complex eigenvalues of the Helmholtz equation (27). Eigenvalues of modes with a significant contribution to the mode expansion (28) are marked blue.

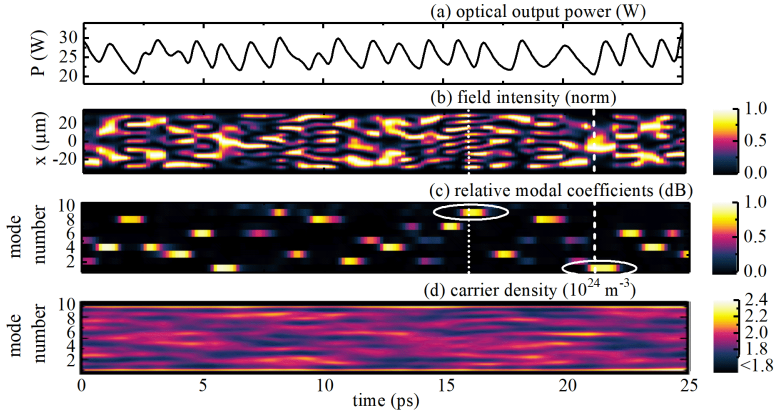

Figure 8: (a) Temporal evolution of the optical output power, (b) pseudo-color mapping of the near-field intensity distribution (normalized to maximum in every time step) and (c) similar mapping of the relative modal coefficients. The vertical lines indicate stages where either a high order mode or the fundamental mode dominates.

In Fig. 8(c) the relative magnitudes $|a_m|^2 / \sum_m |a_m|^2$ of the modal coefficients are displayed versus time as a pseudo-color mapping. Only the 10 modes with the highest gain have a significant contribution to the field (marked blue in Fig. 7). We see that the strong dynamics of the emitted power and near-field intensity (see panels (a) and (b)) is indeed a result of the alternate lasing of a finite number of different lateral modes. At some time instances it can directly be traced back to the dynamic lateral structure of the intensity. For example, at $t = 16.2$ ps (dotted vertical line), the near-field in panel (b) has 9 maxima and accordingly the 9$^{\text{th}}$ mode has the highest contribution to the field, whereas at $t = 21.4$ ps (dashed vertical line) the near-field has one maximum and accordingly the fundamental mode has the highest contribution.

Thus, although no pre-assumptions were made regarding the optical field our result indicates that in the BA lasers considered here a clear mode structure is visible which is neither destroyed by the chaotic dynamics nor by longitudinal effects. Single mode emission becomes unstable above threshold due to lateral spatial hole burning, because each mode saturates the carrier density according to its profile, and consequently the modal gain in those parts of the active layer where the mode intensity is high. The modal gain in other parts rises with current, bringing more modes to threshold, which can be additionally supported by a built-in or thermally induced waveguide. Indeed, recent experiments reveal, that even at currents several times above threshold the lateral modes can be clearly identified by spectrally-resolved near and far-field measurements [29].

4 Application II: Short-pulse operation

First we study an exemplary 10 ns long pulse at an injection current of 150 A, by applying the NHF approximation. The parameters used in the simulation are given in Ref[22]. The bias voltage U is

suddenly turned on and kept constant until pulse end. During the pulse, the thermal index generation rate under the stripe (equation (18)) is positive and strongly fluctuating around a mean value of about 50 ms^{-1} as shown in Fig. 9(a). The corresponding increase of the thermally induced index during the pulse leads to a rise of the effective index below the stripe, whereas the effective index outside the stripe remains approximately unchanged, as depicted by the solid black curves in Fig.10, panel (a) and (b). As a consequence, a thermally induced lateral waveguide is formed under the stripe during the pulse, as displayed in Fig. 10(b). In panels (c) and (d), the near field intensity at the front facet, and the far-field intensity distribution are shown, averaged over 1 ns. The disappearance of side wings in the near field and a change of the far-field intensity are visible.

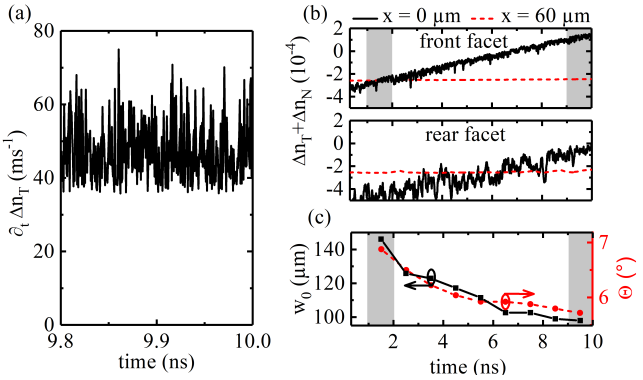

Figure 9: Thermal impact on wave guiding for a 10 ns long 150 A current pulse. (a) Thermal index generation rate of equation (18) during the last 200 ps. (b) Effective index $\Delta n_{\text{eff}} = \Delta n_N + \Delta n_T$ below ($x = 0$ µm) and beside the stripe ($x = 60$ µm) at rear and front facet, respectively. (c) Evolution of the width containing 95% of the power of the near and far fields, averaged over 1 ns.

In effect, a transition from a gain guiding to an index guiding situation occurs during the pulse. This is indicated in Fig. 9, where panel (c) reveals that this transition is accompanied by a shrinking of the widths w_0 and Θ of the lateral near and far-fields containing 95 % of the power.

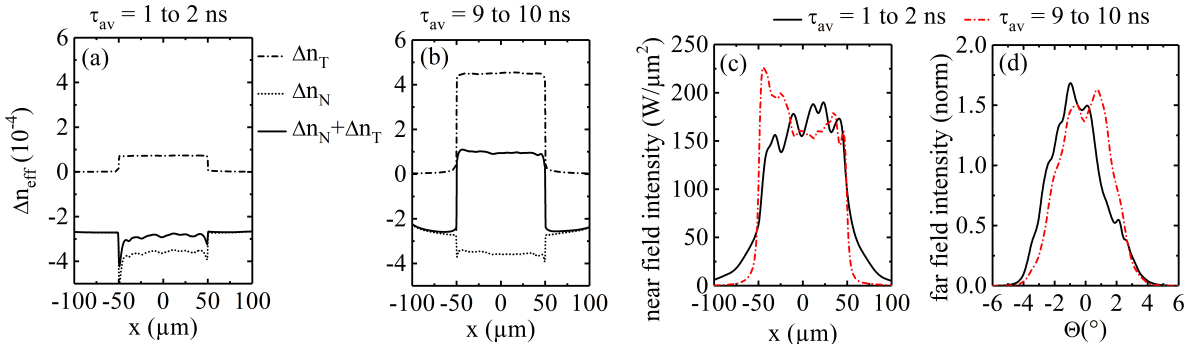

Figure 10: Thermal impact on wave guiding for a 10 ns long 150 A current pulse averaged over the pulse within the time interval 1 to 2 ns and 9 to 10 ns (gray shaded in Fig. 9(b) and (c)). (a) & (b) Lateral profiles of the effective index. (c) Near and (d) far-field intensities.

The described formation of an initial thermally induced waveguide is also detectable in the dependence of time-averaged quantities on the pulse strength. Fig. 11(b) shows a shrinking of the near field width and increased far field angle with increasing injection current (solid curve), compared to the case without thermal wave-guiding (dashed). The mean pulse power, given by the total pulse energy divided by the pulse length, as function of pulse current, in contrast, shows no dependence on wave-guiding for currents up to 150 A, as shown in Fig. 11(a).[2]

The preceding results have been obtained neglecting heat flow. In order to check the validity of this approximation, we have performed the following post processing. We solve the full heat-flow equation

[2]Note, that the neglected changes of parameters with temperature might have an additional influence.

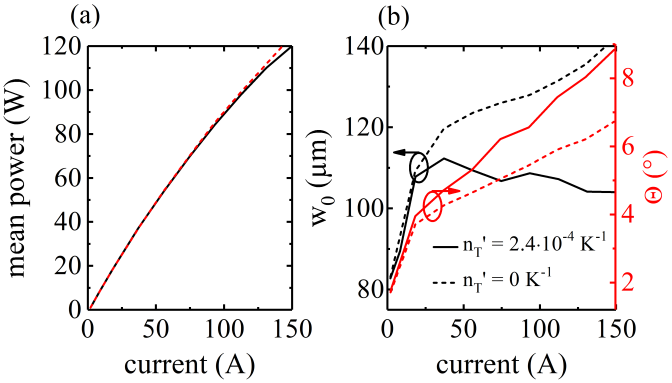

Figure 11: (a) Mean pulse power and (b) near field width (black left axis) and far field angle (red right axis) containing 95 % of the power as function of mean pulse current. Solid curves: with thermal wave-guiding. Dashed curves: without thermal wave-guiding.

(14) where the fluctuating heat source density h at each position is replaced by its average along the whole pulse. Moreover, we continue disregarding inplane heat flow and assume a vertically infinite domain. This is justified because the extensions of lateral and longitudinal inhomogeneities in the heat source densities (cf. Fig. 4) as well as the vertical size of the device are much larger than the expected heat spreading, which is in the range of some hundred nanometers. Under these conditions, the solution of (14) is

$$c_h T(y,t) = \int_{-\infty}^{\infty} d\xi\; h(y+\xi)\,\sqrt{\frac{\kappa_L}{c_h}t}\; w\left(\frac{c_h\xi^2}{4\kappa_L t}\right), \quad w(q) = \left\{\sqrt{q}\,[\mathrm{erf}(\sqrt{q})-1] + \frac{e^{-q}}{\sqrt{\pi}}\right\}. \quad (29)$$

With increasing time, this function deviates more and more from the heat-flow free temperature increase $h(y)t$. Fig. 12(a) shows the situation in the stripe middle and at the pulse end. Here the vertical distribution of the temperature increase is displayed on the left axis. Heat flow reduces the excess temperature in the active layer from 60 K down to 5 K and smoothes the distribution considerably (solid line compared to dashed line). However, to derive the thermally induced index the temperature has to be weighted with the mode profile $|\phi(y)|^2$ shown in Fig. 12(a) on the right axis and integrated over the whole profile. Thus, irrespective of the large temperature differences obtained with and without heat flow, the thermally induced index differs only marginally between the two cases, Fig. 12(b). Thus, the no-heat flow approximation is a reasonable approach to derive the thermal feedback on wave guiding for pulses up to a length of 10 ns.

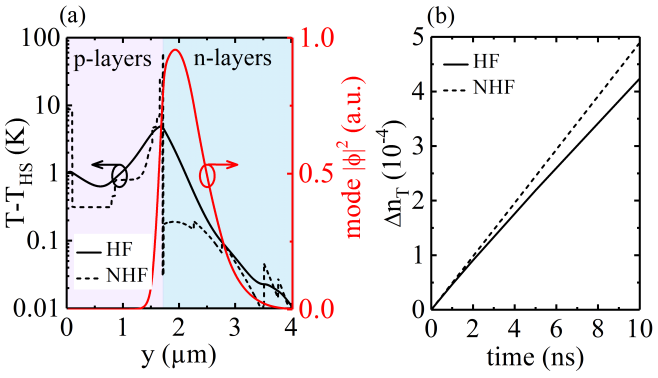

Figure 12: Impact of vertical heat flow. In all cases h is averaged over the pulse. (a) Black left axis: Vertical temperature distributions in the middle of the stripe at the end of the 10 ns pulse with heat flow (HF - black solid) derived from equation (29), and without heat flow (NHF - black dashed). Red right axis: Mode profile $|\phi(y)|^2$. (b) Thermally induced index, eq. (7), versus time in the middle of the stripe with heat flow (HF - black solid) with $T(y,t)$ from eq. (29), and without heat flow (NHF - black dashed), eq. (18).

5 Conclusion

High-power broad-area diode lasers (BALs) exhibit chaotic spatio-temporal dynamics above threshold. Under high power operation heating effects, such as thermal lensing, play an important role. We have proposed a physically realistic and yet numerically applicable thermal model, coupled to a dynamical electro-optical (EO) model for the optical field and carrier dynamics along the quantum-well active zone of the laser. The heat sources obtained with the dynamic EO-solver exhibit strong variations on short time scales, which however have only a marginal impact on the temperature distribution. Two limits have been considered: First, the static HT-problem, with time-averaged heat sources, which is solved iteratively together with the EO solver. Second, under short pulse operation the thermally induced index distribution can be obtained by neglecting heat flow. Although the temperature increase is small, a waveguide is introduced here within a few-ns-long pulse, resulting in significant near field narrowing. We have further shown that a beam propgating in a waveguide structure utilized for BA lasers does not undergo filamentation due to spatial holeburning. This remains a high-dimensional spatio-temporal phenomenon, that can not fully be explained by simplified models, such as the focusing NLS. Moreover, our results indicate that in BALs a clear mode structure is visible which is neither destroyed by the chaotic dynamics nor by longitudinal effects.

References

[1] Čiegis, R., Radziunas, M., and Lichtner, M., "Numerical algorithms for simulation of multisection lasers by using traveling wave model," *Math. Model. Anal.* **13**(3), 327–348 (2008).

[2] Radziunas, M. and Ciegis, R., "Effective numerical algorithm for simulations of beam stabilization in broad area semiconductor lasers and amplifiers," *Math. Model. Anal.* **19**(5), 627–646 (2014).

[3] Radziunas, M., Zeghuzi, A., Fuhrmann, J., Koprucki, T., Wünsche, H. J., Wenzel, H., and Bandelow, U., "Efficient coupling of the inhomogeneous current spreading model to the dynamic electro-optical solver for broad-area edge-emitting semiconductor devices," *Opt. Quantum Electron.* **49**(10), 1–8 (2017).

[4] Radziunas, M., Fuhrmann, J., Zeghuzi, A., Wünsche, H. J., Koprucki, T., Brée, C., Wenzel, H., and Bandelow, U., "Efficient coupling of dynamic electro-optical and heat-transport models for high-power broad-area semiconductor lasers," *Opt. Quantum Electron.* **51**(69) (2019).

[5] Radziunas, M., Botey, M., Herrero, R., and Staliunas, K., "Intrinsic beam shaping mechanism in spatially modulated broad area semiconductor amplifiers," *Appl. Phys. Lett.* **103**(13), 132101 (2013).

[6] Radziunas, M., Herrero, R., Botey, M., and Staliunas, K., "Far field narrowing in spatially modulated broad area edge-emitting semiconductor amplifiers," *J. Opt. Soc. Am. B* **32**(5), 993–1000 (2015).

[7] Zeghuzi, A., Wenzel, H., Wünsche, H.-J., Radziunas, M., Bandelow, U., and Knigge, A., "Modeling of current spreading in high-power broad-area lasers and its impact on the lateral far field divergence," *Proc. SPIE* **10526**, 105261H (2018).

[8] Bree, C., Gailevicius, D., Purlys, V., Werner, G., Staliunas, K., Rathsfeld, A., Schmidt, G., and Radziunas, M., "Chirped photonic crystal for spatially filtered optical feedback to a broad-area laser," *Journal of Optics* **20**(9), 095804 (2018).

[9] Bree, C., Raab, V., Montiel-Ponsoda, J., Garre-Werner, G., Staliunas, K., Bandelow, U., and Radziunas, M., "Beam-combining scheme of high-power broad-area semiconductor lasers with lyot-filtered reinjection: modeling, simulations, and experiments," *J. Opt. Soc. Am. B* **36**(7), 1721–1730 (2019).

[10] Zeghuzi, A., *Analysis of Spatio-Temporal Phenomena in High-Brightness Diode Lasers using numerical Simulations*, PhD thesis, submitted to Humbold University of Berlin (2020).

[11] Zeghuzi, A., Radziunas, M., Wünsche, H.-J., Koester, J.-P., Wenzel, H., Bandelow, U., and Knigge, A., "Traveling wave analysis of non-thermal far-field blooming in high-power broad-area lasers," *IEEE J. Quantum Electron.* **55**(2), 2000207 (2019).

[12] Boyd, R., *Nonlinear Optics*, Academic Press, Elsevier, 3rd ed. (2008).

[13] Gehrig, E. and Hess, O., "Nonequilibrium spatiotemporal dynamics of the Wigner distributions in broad-area semiconductor lasers," *Phys. Rev. A* **57**(3), 2150–2162 (1998).

[14] Böhringer, K. and Hess, O., "A full-time-domain approach to spatio-temporal dynamics of semiconductor lasers," *Prog. Quantum Electron.* **32**, 159–246 (2008).

[15] BALaser: a software tool for simulation of dynamics in broad area semiconductor lasers. http://www.wias-berlin.de/software/balaser/.

[16] Radziunas, M., "Modeling and simulations of broad-area edge-emitting semiconductor devices," *The intl. Journ. of High Performance Computing Applications* **4**(32), 512–522 (2018).

[17] Spreemann, M., Lichtner, M., Radziunas, M., Bandelow, U., and Wenzel, H., "Measurement and simulation of distributed-feedback tapered master-oscillators power-amplifiers," *IEEE J. Quantum Electron.* **45**(6), 609–616 (2009).

[18] Ning, C. Z., Indik, R. A., and Moloney, J. V., "Effective bloch equations for semiconductor lasers and amplifiers," *IEEE J. Quantum Electron.* **33**(9), 1543–1550 (1997).

[19] Wenzel, H. and Zeghuzi, A., "High-Power Lasers," in *Handb. Optoelectron. Device Model. Simul.*, Piprek., J., ed., ch. 33, 15–58, CRC Press, Taylor & Francis Group, 1rst ed. (2017).

[20] Bandelow, U., Gajewski, H., and Hünlich, R., "Fabry-Pérot laser: Thermodynamics - based modeling of edge - emitting quantum well lasers," in *Optoelectronic Devices - Advanced Simulation and Analysis*, Piprek, J., ed., ch. 3, 63–85, Springer, New York (2005).

[21] H. Wenzel and Zeghuzi, A., "High-Power Lasers," in *Handbook of Optoelectronic Device Modeling & Simulation*, Piprek., J., ed., ch. 33, 15–58, CRC Press, Taylor & Francis Group, 1 ed. (2017).

[22] Zeghuzi, A., Wünsche, H.-J., Wenzel, H., Radziunas, M., Fuhrmann, J., Klehr, A., Bandelow, U., and Knigge, A., "Time-dependent simulation of thermal lensing in high-power broad-area semiconductor lasers," *IEEE J. Sel. Top. Quantum Electron.* **25**(6), 1502310 (2019).

[23] Bespalov, V. I. and Talanov, V. I., "Filamentary structure of light beams in nonlinear liquids," *JETP Lett.* **3**(11), 307–310 (1966).

[24] Akhmediev, N. and Ankiewicz, A., *Solitons*, vol. 5 of *Optical and Quantum Electronics*, Chapman & Hall (1997).

[25] Kibler, B., Fatome, J., Finot, C., Millot, G., Dias, F., Genty, G., Akhmediev, N., and Dudley, J. M., "The Peregrine soliton in nonlinear fibre optics," *Nature Physics* **6**, 790–795 (Aug. 2010).

[26] Thompson, G. H. B., "A theory for filamentation in semiconductor lasers including the dependence of dielectric constant on injected carrier density," *Opt. Quantum Electron.* **4**(3), 257–310 (1972).

[27] Hess, O., "Spatio-temporal complexity in multi-stripe and broad-area semiconductor lasers," *Chaos, Solitons and Fractals* **4**(8/9), 1597–1618 (1994).

[28] Marciante, J. R. and Agrawal, G. P., "Nonlinear mechanisms of filamentation in broad-area semiconductor lasers," *IEEE J. Quantum Electron.* **32**(4), 590–596 (1996).

[29] Crump, P., Böldicke, S., Schultz, C. M., Ekhteraei, H., Wenzel, H., and Erbert, G., "Experimental and theoretical analysis of the dominant lateral waveguiding mechanism in 975 nm high power broad area diode lasers," *Semicond. Sci. Technol.* **27**, 045001 (2012).